Contact angle hysteresis in a microchannel: Statics

Metin Hatipogullari[*] and Christophe Wylock

TIPs (Transfers, Interfaces, and Processes), Université Libre de Bruxelles C. P. 165/67,
Av. F. D. Roosevelt 50, B-1050 Brussels, Belgium

Marc Pradas

School of Mathematics and Statistics, The Open University, Milton Keynes MK7 6AA, United Kingdom

Serafim Kalliadasis

Department of Chemical Engineering, Imperial College London, London, SW7 2AZ, United Kingdom

Pierre Colinet

TIPs (Transfers, Interfaces, and Processes), Université Libre de Bruxelles C. P. 165/67,
Av. F. D. Roosevelt 50, B-1050 Brussels, Belgium

We study contact angle hysteresis in a chemically heterogeneous microchannel by tracking static meniscus configurations in the microchannel upon varying the volume of liquid. We first construct a graphical force balance similar to a previous approach by Joanny and de Gennes for this system, though here with a straight contact line. It is shown that hysteresis is induced by wettability gradients above a finite threshold value. This is also visualized in a phase-plane plot enabling to easily predict stick-slip events of the contact line and the occurrence of hysteresis. Above the threshold and for nonoverlapping Gaussian defects, we find good agreement with the expressions by Joanny and de Gennes for the hysteresis amplitude induced by a dilute system of defects. In particular, the hysteresis amplitude is found to be proportional to the square of the defect force and to the defect concentration. For a model sinusoidal heterogeneity, decreasing the ratio between the heterogeneity wavelength and the microchannel gap size brings the system from a subthreshold regime, to a stick-slip dominated regime, and finally to a regime with a quasiconstant advancing and receding angle. In the latter case, the hysteresis amplitude is found to be proportional to the defect force. We also consider an unusual heterogeneity for which the gradients of increasing and decreasing wettability are different. In such a situation breaking the left/right symmetry, whether or not hysteresis is observed will depend on the side the liquid enters the microchannel.

I. INTRODUCTION

Key features of numerous technological innovations across a wide spectrum of applications and their associated industrial processes (coating of substrates is a well-known example) are the dynamics involved with liquid spreading on a solid surface, that is coverage of the surface by displacement, through wetting, of a gas (usually air) by a liquid—see, for example, the comprehensive reviews in Refs. [1–3]. Contact angle hysteresis (CAH) is common place in wetting

---

[*]metin.hatipogullari@ulb.ac.be

processes and it is characterized by a discontinuity between the receding and advancing contact angles [4,5]. It is widely recognized that substrate heterogeneities are the principal source of CAH [5–7]. Such heterogeneities are either chemical or topographical or a combination of the two. Theoretical hydrodynamic analysis of contact line dynamics in the presence of chemical-topographical heterogeneities reveals complex dynamics, such as stick-slip motion and liquid motion due to strong heterogeneity gradients (e.g., uphill motion of a droplet) [8–15]), often in qualitative agreement with experiments. But despite the several developments and considerable attention that CAH has received for several decades, a large number of issues and problems have not been resolved. In particular, including rationally and systematically CAH in theoretical contact line models and/or numerical codes still eludes us [2,16]. This is crucial for the control and optimization of technological processes exploiting CAH. Lack of fundamental understanding of CAH is due in large part to its inherently multiscale nature, a feature that plays a central role in the rapidly growing field of microfluidics [12,17], as the largest typical lengthscales involved are below the capillary length, thus enabling capillary forces to dominate over body forces. For example, the motion of a gas-liquid interface in microsystems, and how it is affected by CAH and related issues such as pinning-depinning, still lack fundamental understanding and rigorous characterization.

A number of theoretical efforts have shown that CAH is rooted in the statics of the system [6,18]. In particular, it has been shown that CAH is related to the rugged free-energy landscape that is induced by the chemical imperfections of the solid, as the associated energy barriers are able to trap the system in metastable configurations that depend on its history [18,19]. This causes the moving contact line (CL) to display hysteresis, even in systems that are either translationally invariant in one direction and can be treated as two-dimensional (2D), in which case the CL is straight [20,21], or in systems for which the CL has a constant curvature by axisymmetry [19].

An intrinsically three-dimensional (3D) approach was adopted in the theory of Joanny and de Gennes [6] which has formed the basis of many theoretical extensions as well as experimental investigations [2]. In their work, the profile of a CL, deformed by a single chemical defect on a substrate, is calculated such as to satisfy the balance of two forces acting on the CL: (i) the excess capillary force exerted by the chemical defect, and (ii) the "elastic restoring force" opposing the deformation of the CL. For a CL close to a "strong" defect (i.e., exerting an excess capillary force above a certain threshold), this force balance is satisfied for two (meta)stable configurations, causing the system to display hysteresis.

In the present study we analyze the advancing and receding motion of the CL in a 2D microchannel with chemically heterogeneous walls. We compare our results with the main fundamental predictions of Joanny and de Gennes [6], including the existence of a threshold value of the heterogeneity strength, below which hysteresis is absent, and the case of a Gaussian defect, where the threshold value shows a logarithmic dependence on the system size and heterogeneity wavelength, and vanishes in the limit of sharp edged (*mesa*) defects. It is important to remark, however, that here we are considering a completely different geometry to the 3D system studied in Ref. [6]. In particular, one of the goals of our work is to verify whether their theoretical predictions are still valid in our case. To this end, we only consider *static hysteresis*, neglecting the following effects: (i) thermal noise which can assist the system to overcome energy barriers [22–25] or external vibrations [19] which if strong enough may mitigate hysteresis [18], and (ii) dynamic effects which can also lead to the occurrence of hysteresis [26].

Another important but still unresolved issue regarding CAH is the question of linking the properties of the substrate disorder to the hysteresis amplitude, which we denote as H. A decisive first step on this question was taken in Ref. [6], where the case of a single strong defect was extended to a regime of sparsely spaced strong defects, and the following scaling law was proposed [2,6,27]:

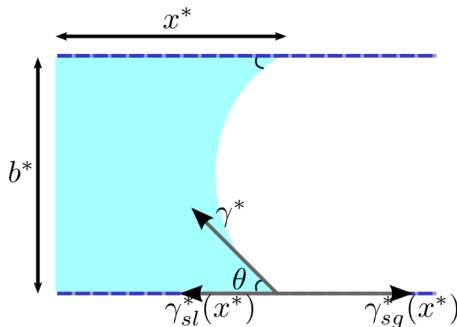$$H = \gamma(\cos \theta_R - \cos \theta_A) \propto \frac{nF_{\max}^2}{\gamma}, \tag{1}$$

FIG. 1. Sketch of the profile geometry for a liquid confined inside a chemically heterogeneous microchannel. γ_{sl}^*, γ_{sg}^*, and γ^* are the wall-liquid, wall-gas, and liquid-gas surface tensions, respectively. The contact angle θ is defined as the angle between the line tangent to the liquid-gas interface at the contact point and wetted area of the walls.

where $F_{\max}$ is the maximum excess of capillary force exerted by a single defect, θ_A and θ_R are the equilibrium advancing and receding contact angles, respectively, γ is the liquid-gas surface tension, and n is the surface density of the defects. The quadratic dependence on $F_{\max}$ and the proportionality with n were verified experimentally and numerically [22,28–30]. However, the extension of this expression to dense defects and to other types of heterogeneities is a challenging question that still remains open [29,31].

Our aim here is precisely to address these issues and provide a quantitative description of CAH. For this purpose we adopt a 2D meniscus in a (2D) microchannel as a model system. To the best of our knowledge, this is the first attempt to address the existence of threshold and scaling laws of hysteresis in 2D systems.

In Sec. II A we introduce the model system, a liquid-gas meniscus in a microchannel with chemically disordered walls and we give the condition for a meniscus in mechanical equilibrium. Adopting the liquid volume as the control parameter, we offer an example in Sec. II B of how CAH can arise in the system. An alternative interpretation to this phenomenon is given in Sec. II C, which involves a graphical force balance, similar to [6]. This similarity is also present in some of the main results. In Sec. III A we show that weak heterogeneities do not produce hysteresis and evaluate the hysteresis threshold for certain wettability distributions. In Sec. III B we explain the qualitatively different regimes of hysteresis upon varying the ratio between the heterogeneity wavelength and the microchannel gap size. We comment on the strong dependence of the threshold on the fluid configuration being considered, and argue that it does not exist for a drop fed by a sufficiently slow (quasistatic) liquid injection, for which all regimes of hysteresis are encountered while the drop grows. For heterogeneities with a strength sufficiently above the threshold, we explore in Sec. III C scaling laws between the parameters of the wettability distribution and H. Finally, conclusions and perspectives are offered in Sec. IV.

II. MODEL FORMULATION AND THEORETICAL FRAMEWORK

A. Definition of the system

We consider a 2D setup consisting of a liquid-gas meniscus moving inside a microchannel (Fig. 1). A gap of width b^* separates two planar, rigid, topographically flat, but chemically heterogeneous walls. This chemical heterogeneity is characterized by a positional dependence of the interfacial tensions γ_{sl}^* and γ_{sg}^* between the walls and the liquid and the gas, respectively. The liquid-gas surface tension γ^* is assumed constant. We thus impose an intrinsic contact angle θ_i distribution, identical on both walls, as

$$\cos(\theta_i(x^*)) = \frac{\gamma_{sg}^*(x^*) - \gamma_{sl}^*(x^*)}{\gamma^*}, \tag{2}$$

where dimensional quantities are denoted with an asterisk.

We assume gravity to be negligible so that the static interface takes a constant curvature (circular arc). Any given pair of the contact line position and contact angle, which we denote as (x^*, θ), fixes the volume of the liquid (per unit length of the contact line):

$$V^* = x^* b^* + b^{*2} f(\theta), \quad f(\theta) = \frac{2\theta - \pi + \sin(2\theta)}{8\cos^2(\theta)}. \tag{3}$$

The free energy F^* of the system, per unit length of the contact line and up to a constant, consists of the three interfacial tensions, integrated along the length on which they act:

$$F^* = \gamma^* l^* + \int_0^{x^*} [\gamma_{sl,u}^*(x^*) - \gamma_{sg,u}^*(x^*)]dx^*$$

$$+ \int_0^{x^*} [\gamma_{sl,b}^*(x^*) - \gamma_{sg,b}^*(x^*)]dx^*, \tag{4}$$

where $l^* = (\pi - 2\theta)/2\cos\theta$ is the dimensional liquid-gas meniscus length, and the subscripts u and b represent the upper and bottom walls, respectively. As we limit our study to identical walls, the two integrals are equal, and

$$F^* = \gamma^* b^* \frac{\pi - 2\theta}{2\cos\theta} - 2\gamma^* \int_0^{x^*} \cos[\theta_i(x^*)]dx^*. \tag{5}$$

To find the extrema of F^* at a fixed volume V_0^*, we minimize the function

$$G^* = F^* + \Lambda[x^* b^* + b^{*2} f(\theta) - V_0^*], \tag{6}$$

with respect to x^* and θ, where Λ is a Lagrange multiplier. This calculation actually yields the natural condition

$$\cos(\theta) = \cos[\theta_i(x^*)], \tag{7}$$

which states that at equilibrium, the meniscus angle must be equal to the local value of the Young's angle, as expected. In the following, we refer to menisci satisfying Eq. (7) as being at *equilibrium configurations*. The volume of such equilibrium configurations is given, in dimensionless form, by

$$V = \frac{V^*}{b^{*2}} = x + f[\theta_i(x)], \tag{8}$$

where we have used b^* as characteristic length scale. Similarly, it is convenient to scale the free energy as

$$F = \frac{F^*}{b^* \gamma^*} = \frac{\pi - 2\theta}{2\cos\theta} - 2\int_0^x \cos[\theta_i(x)]dx. \tag{9}$$

B. Occurrence of contact angle hysteresis

For homogeneous walls ($\theta_i(x) = \theta_0$), V increases linearly with x [Eq. (8)]. For nonconstant $\theta_i(x)$, a nonlinear variation of V with x occurs, but V might still be monotonously increasing with x if variations of θ_i are weak. For sufficiently disordered walls (the condition will be derived in Sec. III A), $V(x)$ increases nonmonotonously, enabling the occurrence of multiple equilibrium configurations for a given volume. In Fig. 2 we consider a model microchannel with periodically varying wetting properties, illustrating the latter case. Specifically, we take $\cos[\theta_i(x)] = 0.2\sin(\frac{2\pi}{0.02}x)$.

For $V = 0.2$, the contact line will adopt one out of seven equilibrium configurations, depending on the history of the system. This odd number of configurations corresponds alternatively to minima (metastable configurations) and maxima (unstable configurations) of the free-energy curve, with the outermost configurations being metastable [see Fig. 2(c)]. These four metastable menisci are drawn in Fig. 2(d). The difference between maxima and neighboring minima can be interpreted as
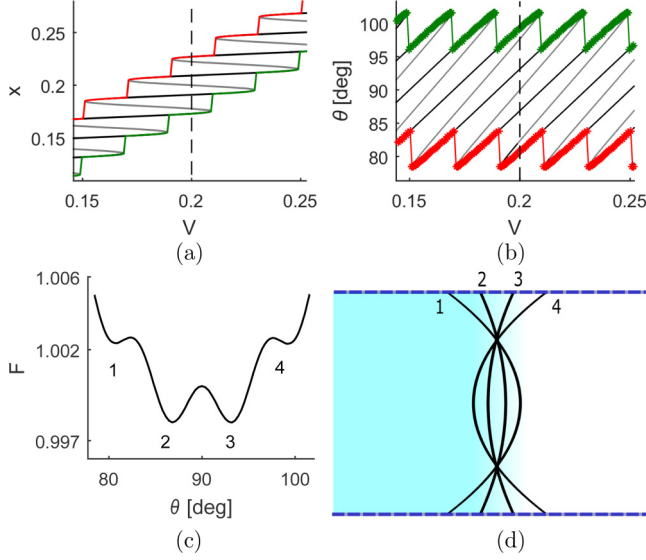
FIG. 2. Example of how contact angle hysteresis occurs in a 2D microchannel with a chemical pattern given by $\cos[\theta_i(x)] = 0.2\sin\left(\frac{2\pi}{0.02}x\right)$. (a) Black and gray: metastable and unstable equilibrium configurations given by Eq. (8); green: presumed advancing trajectory, red: presumed receding trajectory. (b) The corresponding contact angles. (c) Free energy as a function of the actual contact angle for V = 0.2 [indicated with a dashed line in (a) and (b)]; four minima are indicated with numbers. (d) Sketch of the four metastable configurations with V = 0.2, rescaled in the direction orthogonal to the substrate to distinguish clearly the four menisci.

energy barriers which trap the CL in a given metastable configuration [18,32]. The magnitudes of these energy barriers are smallest for the metastable configurations with minimal and maximal θ, in agreement with previous results on an axisymmetric drop [18,32].

Therefore, by imposing that the volume is increasing or decreasing, we obtain the advancing and receding trajectories of the meniscus, respectively, shown as green and red lines in Fig. 2(a). These trajectories are found with the assumption that the system has no ability to overcome energy barriers. For certain values of V, the curve corresponding to equilibrium configurations [black and gray curve in Fig. 2(a)] has a limit (critical) point. At these values of the volume, say V_c, a saddle-node bifurcation takes place, where the local minimum of the free energy F (black) collides with a neighboring maximum (gray), annihilating each other. At these points, the CL suddenly jumps to the closest available metastable state giving rise to slip motion.

The corresponding trajectory followed by θ [Fig. 2(b)] displays the typical experimentally observed sawtooth shapes [33,34] associated with the stick-slip mechanism [11,15,20]. As expected, the advancing contact angle (θ_A) is larger than the receding contact angle (θ_R).

To quantify the global differences between θ_R and θ_A we define the following quantities:

$$\langle\cos\theta_R\rangle = \frac{1}{\Delta V}\int\cos\theta_R\,dV, \tag{10}$$

$$\langle\cos\theta_A\rangle = \frac{1}{\Delta V}\int\cos\theta_A\,dV, \tag{11}$$

$$H = \frac{H^*}{\gamma^*} = \langle\cos\theta_R\rangle - \langle\cos\theta_A\rangle, \tag{12}$$

where $\cos\theta_R$ and $\cos\theta_A$ correspond to the solutions tracked upon, respectively, decreasing and increasing V, and where the choice of ΔV depends on the situation considered. For example, in the case of a periodic heterogeneity, it corresponds to an integer amount of wavelengths. In addition, we

will use the Cassie-Baxter contact angle θ_{CB}, which is given by the average value of $\cos\theta_i(x)$ over the whole microchannel with length L_x (or over a period of the heterogeneity $\theta_i(x)$ in the periodic case):

$$\cos\theta_{CB} = \frac{1}{L_x}\int \cos\theta_i\, dx. \tag{13}$$

C. Graphical force balance

Insight into the phenomenon of CAH can also be obtained by looking at the interplay between the two forces acting on the horizontal direction of the contact line, namely, the spring-type elastic response of the contact line and the force due to the chemical heterogeneities [6]. However, it is important to note that the contact line in our 2D system is straight in the spanwise direction and so the springlike behavior is due to deformations of the meniscus in the cross-stream direction, as shown below, and not to corrugations of the contact line in the spanwise direction as in Ref. [6]. We will see here that the occurrence of hysteresis is generically connected to the multiplicity of solutions (x, θ) for the balance between these forces at a fixed value of V.

The presence of the solid implies a force f_s^* (per unit length of the contact line), in the positive x direction:

$$f_s^* = 2(\gamma_{sg}^* - \gamma_{sl}^*) = 2\gamma^*\cos\theta_i = \gamma^* f_s. \tag{14}$$

At equilibrium, this force is balanced by the *restoring force* f_r^* due to the deformation of the meniscus

$$f_r^* = -2\gamma^*\cos\theta = \gamma^* f_r. \tag{15}$$

Clearly, equilibrium implies $f_s^* + f_r^* = 0$, i.e., $\cos\theta = \cos\theta_i(x)$ as obtained in Eq. (7). Let us now define the deformation of the meniscus by

$$\Delta x = x_V - x, \tag{16}$$

where x_V is the mean position of the meniscus, defined as the position of a straight liquid/gas interface with the same liquid volume. Hence, Δx is geometrically related to θ by:

$$\Delta x = f(\theta), \tag{17}$$

where $f(\theta)$ is given by Eq. (3). The restoring force $f_r = -2\cos\theta$ is an increasing function of the deformation Δx, and can be written as

$$f_r = k(\theta)\Delta x. \tag{18}$$

Therefore, we can interpret the meniscus as a spring with stiffness k that depends only on θ (see Fig. 3), and is given by

$$k(\theta) = \frac{-2\cos\theta}{f(\theta)} = \frac{16\cos^3\theta}{\pi - 2\theta - \sin(2\theta)}. \tag{19}$$

Combining Eqs. (14) and (18), the force balance then reads

$$k(\theta)(x - x_V) = 2\cos\theta_i(x). \tag{20}$$

Figure 4 illustrates this force balance for the case of a single Gaussian-shaped defect:

$$\cos\theta_i(x) = \cos\theta_0 + A_0 \exp\left[-\frac{(x - x_d)^2}{2\sigma^2}\right]. \tag{21}$$

The complete qualitative agreement of Fig. 4 with the graphical construction proposed by Joanny and de Gennes [6], despite the different nature of the spring constant, not only shows the robustness of the idea that a meniscus can be viewed as a spring whose stiffness depends only on θ, but
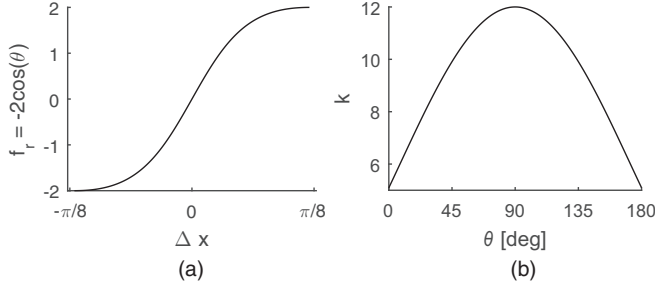
FIG. 3. Spring approximation of the meniscus. (a) The restoring force in dimensionless form as a response to a dimensionless deformation of the contact line, where θ is a plotting parameter varied from 0 to π; (b) meniscus stiffness as a function of the actual angle.

also that the occurrence of hysteresis is generically associated with the existence of multiple static configurations upon varying an experimentally controllable parameter such as the liquid volume. We note, however, that in general, the curves representing f_r are not straight lines as the stiffness depends on the actual contact angle [$\theta = \theta_i(x)$ in Eq. (20)]. By assuming a weak heterogeneity (i.e., $\cos\theta_i(x) = \cos\theta_0 + \Delta\cos\theta_i(x)$ with $|\Delta\cos\theta_i(x)| \ll 1$), the force balance may be linearized by noting that $x - x_V = -f[\theta_i(x)] \simeq -f(\theta_0) + f'(\theta_0)\Delta\cos\theta_i(x)/\sin(\theta_0)$, which is recast as

$$\frac{\sin(\theta_0)}{f'(\theta_0)}(x - \tilde{x}_V) = \Delta\cos\theta_i(x), \tag{22}$$

with

$$\tilde{x}_V = x_V - f(\theta_0). \tag{23}$$

Depending on the particular situation being considered, such a linearized force balance may be sufficient to describe the hysteresis behavior.
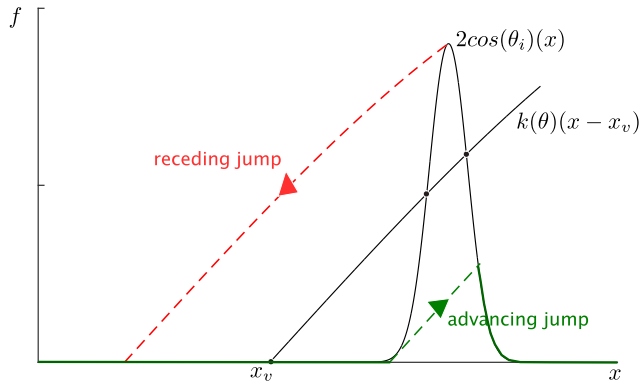

FIG. 4. Example of graphical force balance with $\theta_0 = \frac{\pi}{2}$, $A_0 = 0.9$, and $\sigma = 0.01$. For a range values of x_V in the vicinity of the defect, up to three solutions are obtained for x (indicated with black dots). In this range, a different path of solutions is followed by the advancing CL (green) and receding CL (red). Both directions require a jump which is indicated with a striped line.

III. RESULTS

A. Hysteresis threshold and phase-plane plots

As is evident from Fig. 2, for multiplicity of equilibrium configurations for a given volume to occur, there must be at least one critical contact line position x_c, where a saddle-node bifurcation takes place. At one of these points, the meniscus jumps either forward in an advancing path or backwards in a receding path, as the volume varies. Alternatively, we can see these critical points as maxima and minima, respectively, of $V(x)$. Making use of Eq. (3) we can hence write

$$V'(x_c) = 1 + \frac{\partial f(\theta_i)}{\partial \theta_i} \frac{\partial \theta_i}{\partial x}\bigg|_{x=x_c} = 0, \tag{24}$$

where $V'(x_c) = \frac{dV}{dx}\big|_{x=x_c}$. Denoting $\hat{\theta}_{ic} \equiv \theta_i'(x = x_c)$ and rearranging the above equation, we get

$$\hat{\theta}_{ic} = -\frac{1}{\frac{\partial f(\theta_i)}{\partial \theta_i}} = \frac{2\cos^2\theta_i}{\left(\frac{\pi}{2} - \theta_i\right)\tan\theta_i - 1}. \tag{25}$$

Therefore, at critical points, the *wettability gradient* $\hat{\theta}_{ic}$ exhibits a generic behaviour that does not depend on the particular form of $\theta_i(x)$ but only on the given value of θ_i. The points where the curve of $\theta_i'(x)$ versus $\theta_i(x)$ crosses the generic curve $\hat{\theta}_{ic}(\theta_i)$ correspond to the critical values of x at which jumps occur (either forward or backward). Thus, for a given distribution $\theta_i(x)$, visualizing both curves in a *phase-plane plot* will enable predicting whether and where the CL will jump. As θ_i is physically limited between 0 and π, we have that $\hat{\theta}_{ic}(\theta_i)$ is limited between -2 (for $\theta = 0$ and π) and -6 (for $\theta = \frac{\pi}{2}$). Importantly, the negative sign of $\hat{\theta}_{ic}$ implies that an advancing (receding) meniscus can only start jumping from a position at which the wettability is increasing with increasing x (decreasing with decreasing x).

Another point to remark is that hysteresis occurs only if the strength of a (smooth) heterogeneity is above a finite *threshold* (a similar observation was reported in [6], albeit in a different physical system). If the condition $\theta_i'(\theta_i) = \hat{\theta}_{ic}(\theta_i)$ is not satisfied for any x, then stick-slip does not occur and the same path of static solutions is followed during advancing and receding. These behaviours are illustrated in the following.

1. Smooth heterogeneities

We consider two examples for $\theta_i(x)$, namely, a single Gaussian-shaped defect with amplitude A_0, width σ, and located at x_d:

$$\theta_i(x) = \theta_0 + A_0 \exp\left[-\frac{(x - x_d)^2}{2\sigma^2}\right], \tag{26}$$

and a periodic heterogeneity with amplitude A_0 and wavelength λ:

$$\theta_i(x) = \theta_0 + A_0 \sin\left(\frac{2\pi x}{\lambda}\right). \tag{27}$$

As just remarked, if condition Eq. (25) cannot be satisfied, a multiplicity of static solutions and hysteresis cannot occur. This is the case when $\theta_i'(x)$ is not negative enough, which is certainly true if $\min[\theta_i'(x)] > -2$. For the Gaussian defect Eq. (26) this condition leads to the relation $\frac{|A_0|}{\sigma} < 2\sqrt{e}$, and for the sinusoidal heterogeneity to $\frac{|A_0|}{\lambda} < 1/\pi$.

However, condition Eq. (25) is certainly satisfied if $\min(\theta_i'(x)) < -6$, which leads to the conditions $\frac{|A_0|}{\sigma} > 6\sqrt{e}$ for the Gaussian defect, and $\frac{|A_0|}{\lambda} > 3/\pi$ for the sinusoidal heterogeneity Eq. (27). For values of $\frac{|A_0|}{\sigma} \in (2\sqrt{e}, 6\sqrt{e})$ [or $\frac{|A_0|}{\lambda} \in (1/\pi, 3/\pi)$] hysteresis may or may not occur, depending on the background contact angle θ_0. In that respect, note that condition Eq. (25) is more difficult to satisfy for a CA of $\frac{\pi}{2}$, because this is the angle around which $\hat{\theta}_{ic}$ is most negative.
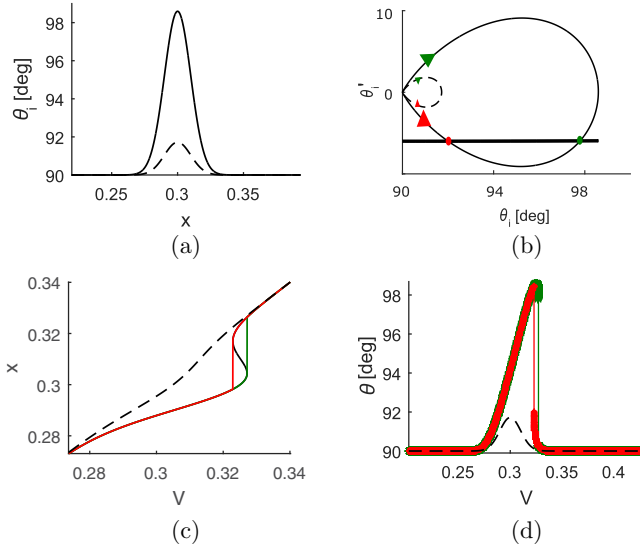
FIG. 5. Comparison of behavior above ($A_0 = 0.15$, full lines) and below ($A_0 = 0.03$, dashed lines) threshold for a single defect [Eq. (26)] with $\sigma = 0.01$ and $\theta_0 = \frac{\pi}{2}$). (a) Intrinsic contact angle distributions; (b) phase plots of both distributions, the thick line represents $\hat{\theta}_{ic}$ (it is a curve which appears straight in the present case). The green (red) arrow and dot represent, respectively, the sense of circulation and the start of the jump for an advancing (receding) CL; (c) CL position followed in advancing (green) and receding (red) trajectory above the threshold, and below the threshold (dashed); (d) contact angle corresponding to these trajectories.

We thus conclude that the quantity $\frac{|A_0|}{\sigma}$ (or $\frac{|A_0|}{\lambda}$) determines whether hysteresis occurs or not, i.e., it is the gradient of wettability that matters. In particular, for a given defect amplitude A_0, hysteresis will always be observed at sufficiently small defect size (compared to the microchannel gap).

Figure 5 depicts a comparison between two cases that are below and above the threshold for a single Gaussian defect [see Fig. 5(a)]. As is evident from the phase plot [Fig. 5(b)], the system starts at the origin and moves clockwise along a closed trajectory for an advancing CL (increasing x), or anticlockwise for a receding CL (decreasing x). If the defect is weak (dashed line), the phase plot does not intersect the generic line $\hat{\theta}_{ic}(\theta_i)$. However, for the stronger defect (full line), there are two intersections on the phase plot, which correspond to the minimum (left) and maximum (right) of $V(x)$ [cf. Fig. 5(c)]. These are the points at which the receding and advancing jump start, respectively. The ending points of the jumps are found with the assumption of the constant volume, corresponding to a case where the rate of externally imposed volume variation is negligible compared to the velocity of the jumps. For values of the volume in between the values corresponding to the jumps, multiple equilibrium states exist and the system will choose one depending on whether the volume has been increasing or decreasing [Fig. 5(c)]. More specifically, the advancing CL follows the branch corresponding to lower x, while the receding CL follows the branch corresponding to higher x. The middle branch is unstable as it corresponds to maxima of the free energy (as in Fig. 2). The contact angles corresponding to the two branches are shown in Fig. 5(d), revealing that when increasing V (green), the CL first sticks on the hydrophobic defect, causing θ to increase progressively, and then slips, corresponding to a sudden decrease of θ. When decreasing V (red), the CL almost directly slips over the hydrophobic defect, corresponding to a sudden increase of θ, and then sticks, causing θ to decrease progressively. Both for the hydrophobic case considered here, and for a hydrophilic defect, jumps correspond to a decrease of θ when increasing V, and to an increase of θ when decreasing V.
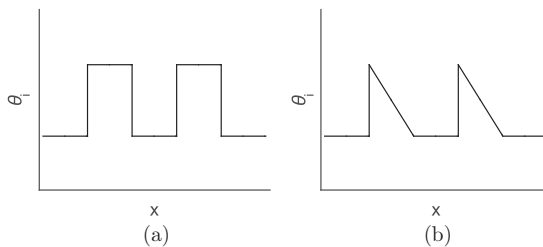
FIG. 6. Examples of sharp edged heterogeneities. (a) Symmetric, involving the same steps of increasing and decreasing wettability; (b) nonsymmetric, having a different slope for increasing and decreasing wettability.

For the periodic heterogeneity given by Eq. (27), we observe a similar behavior in terms of the threshold-dependence of hysteresis. We will consider this case in more detail in Sec. III B.

2. Sharp heterogeneities

We now consider sharp-edged defects, or *mesa defects* adopting the term coined by Joanny and de Gennes [6]. In the limit case of *symmetric* mesa defects—i.e., defects involving both a steplike increase and decrease in wettability, as shown in Fig. 6(b)—$\theta_i'(x)$ will reach both plus and minus infinity, crossing the generic curve $\hat{\theta}_{ic}$ in between. Hence, such defects, featuring infinitely large wettability gradients, always generate hysteresis, as was predicted by Joanny and de Gennes [6]. Asymmetric heterogeneities, however, of which the intrinsic CA decreases too slowly with increasing x ($\min[\theta_i'(x)] > -2$), do not generate hysteresis, even if the increases of CA are steplike. We illustrate this with the example of a triangular heterogeneity with amplitude A_0 and wavelength λ given by

$$\theta_i(x) = \theta_0 + \frac{2A_0}{\pi} \arctan\left[\cot\left(\frac{\pi x}{\lambda}\right)\right] \tag{28}$$

and shown in Fig. 7(a). Any negative value of A_0 implies step-like decreases of the intrinsic CA with increasing x, which give rise to hysteresis. For a positive value of A_0, however, no hysteresis will occur if $\{\min[\theta_i'(x)] > -2\} \equiv -\frac{2A_0}{\lambda} > -2$, or $0 < A_0 < \lambda$. Figure 7 is an example of such a case. On the contrary, the same heterogeneity with an inversed sign of A_0 does generate hysteresis (Fig. 8). For this heterogeneity, inverting the sign of A_0 is equivalent to inverting the sign of the coordinate x. Therefore, the situation in Fig. 8 can be obtained in exactly the same microchannel as in Fig. 7, by simply placing the liquid inlet at the right-hand side. Hence, for a microchannel with this particular type of heterogeneity, whether or not the system will suffer hysteresis and stick-slip, will depend on the side from which the liquid enters.

This analysis shows that the existence and nature of the threshold does not only depend on the wetting properties of the substrate $\theta_i(x)$, but also on the particular liquid configuration (in the Appendix we will contrast our predictions with the case of a droplet). However, recall that all lengths, and hence the typical length scale of the heterogeneity, are normalized with the gap width separating the two plates of the microchannel. As a result, the weak Gaussian-shaped defect corresponding to the dashed lines in Fig. 5 would be a strong defect in a microchannel with a gap size that is five times larger. This points to the importance of the overall length scales of the system, something that deserves more attention and was not considered in the work by Joanny and de Gennes [6], nor was it discussed in the more recent review by Bonn *et al.* [2].

B. From large to small heterogeneity length scale: The macroscopic limit

Here we discuss qualitatively the effects on hysteresis of the ratio λ between the characteristic lengthscale of the heterogeneity and the gap size of the microchannel (which is constraining the
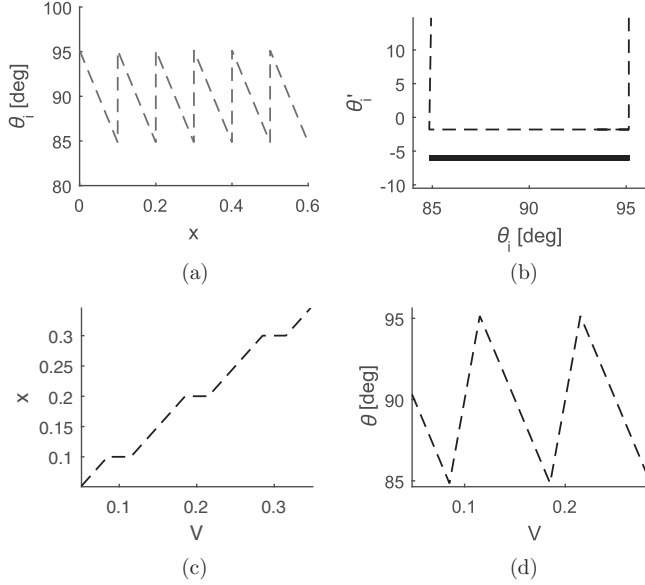
FIG. 7. Subthreshold triangular heterogeneity [Eq. (28) with $A_0 = 0.09$, $\theta_0 = \pi/2$ and $\lambda = 0.1$]. (a) Intrinsic contact angle distribution; (b) phase-plane plot, the thick line represents $\hat{\theta}_{ic}$; (c) CL position as a function of volume (same for advancing and receding); (d) contact angle corresponding to this trajectory.

liquid-vapor interface in this configuration), by looking at a periodic distribution of the spreading coefficient of the walls as a model prototype

$$\cos[\theta_i(x)] = A_0 \sin\left(\frac{2\pi}{\lambda}x\right). \tag{29}$$

This heterogeneity is different to that given by Eq. (27), because there we had imposed for simplicity a distribution for $\theta_i(x)$, as opposed to the spreading coefficient which is proportional to $\cos[\theta_i(x)]$ and which gave a simple analytical result for the value of the threshold, whereas here we want to obtain a scaling law for the hysteresis force. The results for this case are presented in Fig. 9. For a given value of A_0 and when λ is sufficiently high (see first column of Fig. 9) the system is in a subthreshold regime (i.e., the gradient $|A_0|/\lambda$ is too small). Although the contact angle varies with volume, hysteresis is absent. In particular, we observe that for each volume we find a unique static configuration (x, θ), the phase-plane plot of the heterogeneity does not intersect the generic curve $\hat{\theta}_{ic}$, and the advancing and receding CL follow the same path, in clockwise and anticlockwise directions, respectively. The CA takes all possible values imposed in the distribution in Eq. (29) in both the advancing and receding directions. Hence in this regime, advancing CAs lower than the Cassie-Baxter angle (here equal to 90°) are possible, and receding CAs higher than the Cassie-Baxter one, are possible.

If we decrease λ by a factor of three (second column of Fig. 9) by, e.g., increasing the gap width by the same factor, the system is then in a regime in which hysteresis occurs. We find that for most volumes there exists a unique static configuration (x, θ), but in certain ranges three static solutions are found. At these points, the solution branch followed by the system will depend on whether the CL advances or recedes. The contact angle of an advancing CL is on average higher. At the intersections between the phase plot of the heterogeneity and the generic curve $\hat{\theta}_{ic}$, the contact line jumps (slips) to a point which has the same volume if we assume that such jumps occur instantaneously compared to the rate of volume variation. In the phase-plane plot, an advancing CL follows a different path than a receding CL.
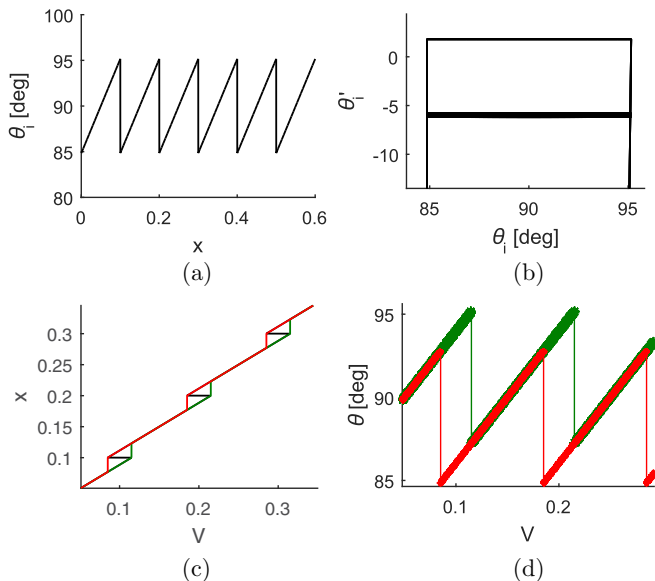
FIG. 8. Triangular heterogeneity which generates hysteresis [Eq. (28) with $A_0 = -0.09$ and $\lambda = 0.1$]. (a) Intrinsic contact angle distribution; (b) phase-plane plot, the thick line represents $\hat{\theta}_{ic}$; (c) CL position as a function of volume for (black: all static solutions, green: followed during advancing, red: followed during receding); (d) contact angle corresponding to these paths.

A further decrease in λ (third column of Fig. 9) increases the number of static solutions (x, θ) for a given volume. The path followed by an advancing CL is now totally different than the one followed by a receding CL. When λ decreases, jumps get smaller and occur more frequently. The contact angles follow sawtooth shapes which get further separated. The advancing CAs are at all times higher than the Cassie-Baxter angle, while the receding CAs are lower. The bows followed in the phase diagram are separated further.

In the limit $\lambda \to 0$, which we refer to hereafter as the *macroscopic limit*, the number of static solutions (x, θ) at any given volume starts becoming arbitrarily high. This situation is represented for $\lambda = 0.001$ in the fourth column of Fig. 9. The CL advances with a nearly constant contact angle, corresponding in this case to the maximum of the imposed distribution, and recedes with a nearly constant contact angle (which is the minimum of the imposed distribution). The sawtooth amplitude of the contact angle is below $0.3°$ and hysteresis is maximum.

In the above analysis, we have assumed that the system has no ability to overcome energy barriers, which are also affected by varying λ. A lower value of this parameter increases the amount of extrema in the energy landscape for a fixed volume [Figs. 10(a) and 10(b)]. We define the maximum energy barrier E_{BM} which needs to be overcome in order to attain the most stable contact angle θ_{MS}, as indicated on Fig. 10(b). E_{BM} is found to decrease with λ^{-1} and reaches a value of the order 10^{-4} for $\lambda = 0.001$ [Fig. 10(c)]. The most stable angle [Fig. 10(d)], approaches the Cassie-Baxter angle ($90°$). This result was previously reported in Refs. [35,36] for a configuration of a drop much larger than the heterogeneity wavelength.

C. Scaling laws of the hysteresis force

1. Near threshold behavior

Let A_{0c} be the threshold value for the amplitude of the chemical defect. For $A_0 = A_{0c}$, at a certain contact line position, say x_0, we have that the volume satisfies
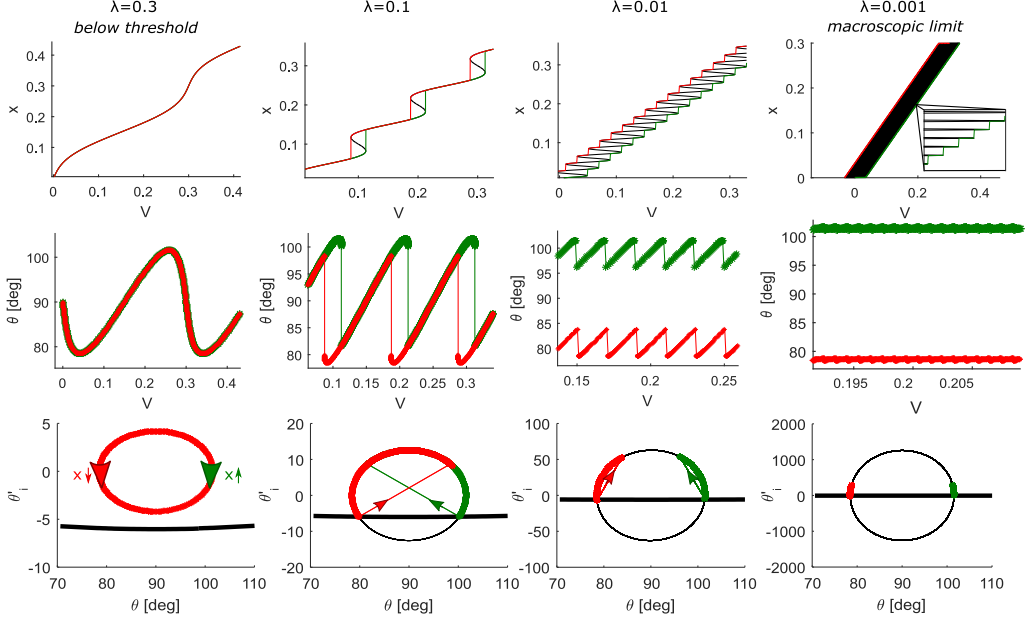
$$V'(x_0) = V''(x_0) = 0. \tag{30}$$

FIG. 9. Qualitatively different regimes of hysteresis for the microchannel (assuming the system has no ability to overcome any energy barriers) caused by a model periodic heterogeneity given in Eq. (29) with $A_0 = 0.2$. The columns represent different values of λ, from left to right: 0.3, 0.1, 0.01, and 0.001. On the upper row: black, equilibrium configurations; green, presumed advancing path; red, presumed receding path. On the middle row: the contact angle of the equilibrium configurations encountered in the advancing (green) and receding (red) path. Lower row: phase plots of the distribution in black, the thick line represents $\hat{\theta}_{ic}$, for an advancing contact line (green), the system moves in a clockwise fashion, while for a receding contact line (red), the motion is counterclockwise, as indicated with the large arrows. The small arrows (with the same color code) indicate jumps.

Consider the deviations from this point for the quantities

$$A_0 = A_{0c} + \mu, \quad x = x_0 + \tilde{x}. \tag{31}$$

By using Eq. (30), we expand the volume for $\mu \ll 1$ and $\tilde{x} \ll 1$ as

$$V = x + f(\theta_i(x, A_0)) \approx V_0 + c_1\mu + c_2\mu\tilde{x} + c_3\tilde{x}^3. \tag{32}$$

The extrema of V are then given by

$$\frac{dV}{dx} = 0 = c_2\mu + 3c_3\tilde{x}^2, \tag{33}$$

the solutions of which, assuming $c_2 c_3 < 0$, are

$$\tilde{x}_\pm = \pm\left(-\frac{c_2\mu}{3c_3}\right)^{1/2} \propto \mu^{1/2}. \tag{34}$$

Inserting the above values into Eq. (32), we obtain

$$V_{\max} - V_{\min} \propto \mu^{3/2}, \tag{35}$$

where $V_{\max} = V(x_+, A_0)$ is the relative maximum of the volume at which the CL jumps in an advancing path, and $V_{\min} = V(x_-, A_0)$ is the relative minimum of the volume, at which the CL
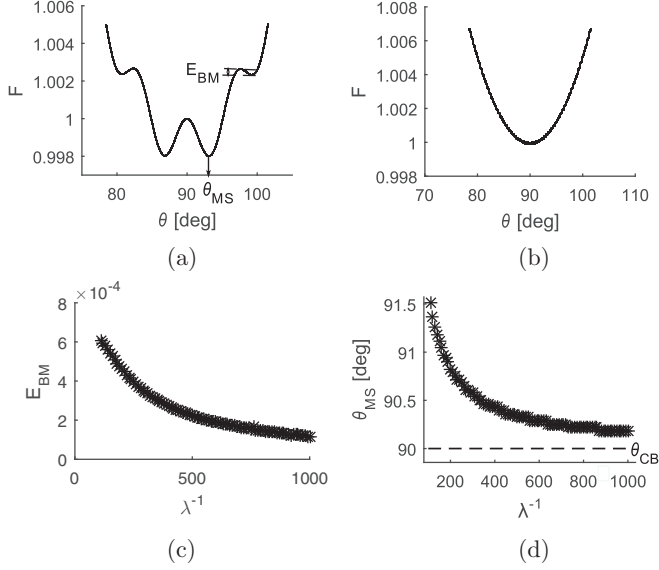
FIG. 10. Change of rugged energy landscape upon varying λ in Eq. (29) with $A_0 = 0.2$ with a fixed volume $V = 0.2$. (a) and (b): Energy landscape $F = \frac{F^*}{\gamma^* b^*}$ as a function of actual contact angle for resp. $\lambda = 0.02$ and $\lambda = 0.001$. The most stable contact angle θ_{MS} and the maximal energy barrier E_{BM} to reach it are indicated with arrows on (a). As the energy landscape is symmetric about 90°, these quantities are measured from the right side; (c) The maximum energy barrier to reach the most stable contact angle versus λ^{-1}. (d) Most stable contact angle versus λ^{-1}. The dotted line represents the Cassie-Baxter angle.

jumps in a receding path. The magnitude of the jumps of the force scales as

$$\delta f \propto \cos[\theta_i(x_-, A_0)] - \cos[\theta_i(x_+, A_0)] \propto \theta_i(x_+, A_0) - \theta_i(x_-, A_0)$$
$$\propto x_+ - x_- \propto \mu^{1/2}. \tag{36}$$

According to definitions Eqs. (10)–(12), the hysteresis H is directly related to the area between the curves of $\cos\theta_R$ and $\cos\theta_A$ versus V. Combining Eqs. (35) and (36) we thus find that close enough to the threshold, the hysteresis amplitude scales as

$$H \propto \mu^2 \propto (\delta f)^4. \tag{37}$$

In the following, we explore numerically the emergence of scaling laws. We first focus on the case of hysteresis caused by an array of wetting defects, with emphasis on the dilute limit at which we have a minimum number of equilibrium configurations for a given volume.

2. Dilute system of wetting defects

Consider a single Gaussian-shaped defect:

$$\cos\theta_i(x) = \cos\theta_0 + A_0 \exp\left[-\frac{\left(x - \frac{L_x}{2}\right)^2}{2\sigma^2}\right], \tag{38}$$

where we fix $\theta_0 = \frac{\pi}{2}$. We assume $A_0 > 0$, i.e., a defect which is more wettable than the rest of the surface, and vary the amplitude A_0 over 400 values, logarithmically spaced in the interval between 0.001 and 0.99, for four values of the defect width σ. The computational domain L_x is fixed to a dimensionless length of unity and discretized in sections of $\Delta x = 10^{-5}$. With this length the whole pinning-depinning process is captured for all considered defect widths. For each value of σ,
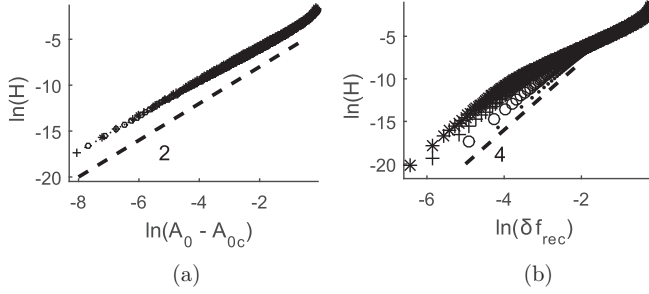
FIG. 11. Logarithmic plots of the dimensionless hysteresis force $H = \langle \cos\theta_R - \cos\theta_A \rangle$, for a single, wetting defect, for $\theta_0 = \pi/2$ for four values of σ: 0.01 ($*$), 0.005 ($+$), 0.002 (o), and 0.001 (.), as a function of (a) the defect amplitude, and (b) the fluctuation δf_{rec} of $\cos\theta_R$ during the jump. The dashed lines with slopes two and four are drawn to guide the eye.

a threshold amplitude A_{0c} is calculated numerically as the minimum A_0 for which the phase plot of the heterogeneity intersects the generic line (Sec. III A).

Figure 11(a) shows that hysteresis depends only slightly on the width of the defect. The effect of defect amplitude A_0 on the hysteresis is twofold. A larger A_0 does not only imply a larger difference between the CA on the defect and the background angle, but also larger jumps (see the graphical force balance in Fig. 4), hence a larger range of V during which the CA differs from the background angle. Near the threshold [see Eq. (37)] but also far from it, the hysteresis is found to scale as

$$H \propto (A_0 - A_{0c})^2, \tag{39}$$

where A_{0c} is the threshold amplitude depending on σ, which is 0.04945 and 0.00495 for the broadest and sharpest defect, respectively. As the maximum excess force $F_{s,\max}^*$ exerted on the contact line by the defect is proportional to $\gamma^* A_0$, we may write for the dimensional hysteresis force H^*

$$H^* = \gamma^* H \propto \frac{F_{s,\max}^{*2}}{\gamma^*}, \tag{40}$$

where A_{0c} has been assumed negligibly small against A_0, e.g., in the macroscopic limit $\sigma \to 0$. This scaling law is in agreement with previous theoretical and numerical predictions [6,30] and experiments [28], though in different configurations to the one studied here.

It is important to emphasise that in fact, the hysteresis caused by the wetting defect is mainly due to the increase of $\langle \cos\theta_R \rangle$ when A_0 increases, while $\langle \cos\theta_A \rangle$ stays nearly constant (see also the graphical force balance in Fig. 4). This is consistent with experimental findings [22,34,37] on surfaces with controlled chemical defects and can be understood by the fact that a wetting defect primarily affects [4] or more specifically pins [34] the CL in the receding direction. Figure 11(b) shows that close enough to the threshold, the hysteresis amplitude scales with the fluctuation of the force caused by a jump to the power four, also in agreement with Sec. III C 1. Further from threshold, no clear scaling behaviour can be observed.

We note that the absolute value of H depends on the domain size. An increasing system size indeed enhances the dilution of the effects of the defect by the homogeneous background. This can be avoided by considering an array of such defects. We thus impose an array of N equally spaced and identical wetting defects,

$$\cos\theta_i(x) = \cos\theta_0 + A_0 \sum_{i=1}^{N} \exp\left[-\frac{(x - x_{di})^2}{2\sigma^2}\right], \tag{41}$$

where $x_{di} = i\frac{L_x}{N+1}$. Figure 12 shows that for low enough N, the hysteresis force is directly proportional to N, which is in agreement with experiments [29] and the proposed scaling law for
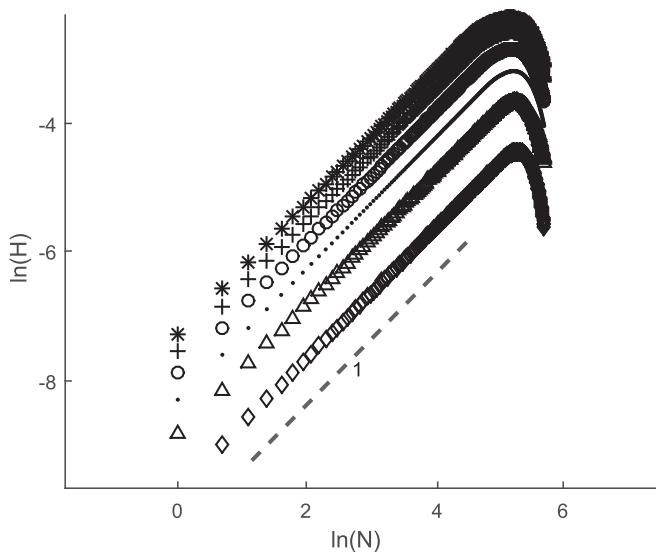
FIG. 12. Logarithmic plot of the dimensionless hysteresis force $H = \langle \cos\theta_R \rangle - \langle \cos\theta_A \rangle$ for an array of equally spaced, identical wetting defects with width $\sigma = 0.01$ as a function of the amount of defects for six values of A_0: 0.075 ($\diamond$), 0.1 ($\triangle$), 0.125 (.), 0.15 (o), 0.175 (+), and 0.2 ($*$).

the hysteresis caused by a dilute system of defects [2,6,27]:

$$H^* = \gamma^*(\cos\theta_R - \cos\theta_A) \propto \frac{n(F^*_{\max})^2}{\gamma^*}. \tag{42}$$

The effects of the individual defects are simply additive as long as they are independent (nonoverlapping). As the density of defects N is increased, however, this proportionality no longer holds as the stick-slip of the CL on a defect is affected by neighboring defects. More specifically, the jumps of the CL do not end anymore on homogeneous parts between defects, but on other defects. This *shadowing* effect increases with N, decreasing the slope on the plot. For N above 150, the defects start overlapping and hysteresis even starts decreasing as the substrate becomes less heterogeneous, though with a shifted background value.

3. Periodic heterogeneity

In our last example, we consider a periodic heterogeneity of the form:

$$\cos[\theta_i(x)] = A_0 \sin\left(\frac{2\pi}{\lambda}x\right). \tag{43}$$

The computational domain has a length of 20λ. We vary A_0 over 100 logarithmically spaced values between the threshold value and 0.89, and λ over 8 logarithmically spaced values, between 10^{-4}, which is indistinguishably close to the macroscopic limit, and 0.578. The ranges of V over which the contact angles are integrated [in Eqs. (10) and (11)] start and end with the value at the CL jumps.

The threshold amplitude A_{0c} is 0.302 for the highest λ and 9.56×10^{-5} for the lowest, satisfying A_{0c}/λ constant. We find that the scaling exponent depends on the wavelength λ as follows. For the lowest values of λ the hysteresis force is proportional to the defect force. For broader heterogeneities, the scaling exponent increases with λ and reaches a value of around two when λ is of the order of one (see Fig. 13). We then write
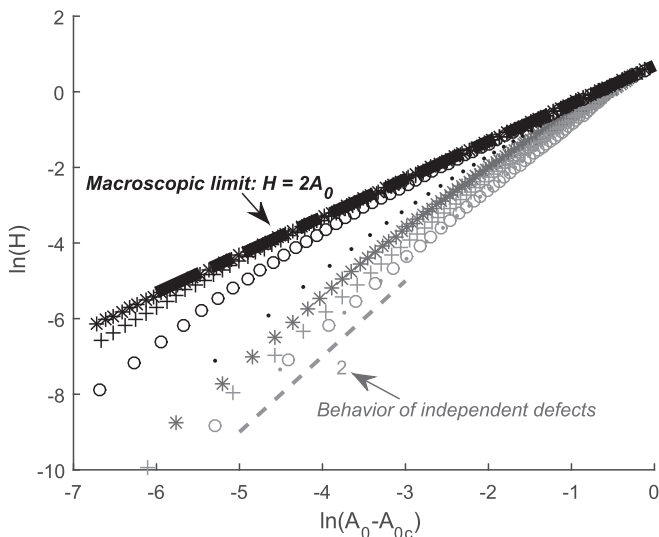
$$H^* \propto F^*_{s,\max}, \tag{44}$$

FIG. 13. Logarithmic plot of the dimensionless hysteresis force $H = \langle\cos\theta_R\rangle - \langle\cos\theta_A\rangle$ as a function of the heterogeneity amplitude for a periodic heterogeneity with $\theta_0 = \pi/2$ and 8 values of λ. Black symbols correspond to small wavelengths: $\lambda = 1.\ 10^{-4}$ ($*$), $8.\ 10^{-4}$ ($+$), $5.80.\ 10^{-3}$ (o), $4.44.\ 10^{-2}$, and (.). Gray symbols correspond to large wavelengths: $\lambda = 0.1$ ($*$), 0.178 ($+$), 0.316 (o), and 0.562 (.). The black dashed line (collapsing with data) corresponds to the macroscopic limit. The gray dashed line with slope two is drawn as visual aid.

for $\lambda \to 0$. The linear behavior corresponds exactly to the macroscopic limit ($\lambda = \frac{\lambda^*}{b^*} \to 0$), in which the advancing and receding angle are nearly constant and equal to the minimum and maximum of the imposed distribution ($H \to 2A_0$), respectively. Also, for this infinitely sharp heterogeneity, the threshold amplitude vanishes ($A_{0c} \to 0$). This limit is plotted in black dashed lines and collapses with the data for sufficiently low λ, and at sufficiently high $A_0 - A_{0c}$ (although A_0 has an upper bound $A_0 = 1$, see Eq. (43)). This suggests that the value of λ below which this limit is reached depends on A_0.

Away from this limit, i.e., for higher λ, the system is in a regime of observable stick-slip (see Sec. III B) where the difference between the advancing and receding angle depends on V. The exponent is larger than the one found for this regime and is due to the same effect as in the case of a single defect (Sec. III C 2): An increase of the amplitude of the heterogeneity A_0 increases both the difference between the advancing and receding angle at the value of V at which the jumps occur, and the range of V during which these angles differ.

IV. CONCLUSIONS AND PERSPECTIVES

We have analyzed in detail stick-slip motion and CAH of a liquid-gas meniscus in a chemically heterogeneous microchannel of fixed gap width by tracking stable and metastable states upon varying the liquid volume and for a wide range of heterogeneity distributions. To the best of our knowledge, this is the first time that such a study has been undertaken. Our goal has also been to examine to what extent previous results of wetting hysteresis hold in the present configuration.

We showed that the stick-slip mechanism can be studied using phase-plane plots of the heterogeneity. Weak heterogeneities do not produce hysteresis, a threshold for the heterogeneity strength is required. For values of the heterogeneity strength sufficiently above the threshold, we find good agreement with the previously reported expressions for the hysteresis amplitude for a diluted system of defects, even though the geometry and approach used here are notably different. For a

model sinusoidal heterogeneity, we have found that the ratio between the heterogeneity wavelength and the liquid-gas interface length is a key parameter determining the qualitative aspects of the hysteresis. More specifically, decreasing gradually this ratio brings the system from a subthreshold regime (i.e., no hysteresis), to a stick-slip dominated regime, and ultimately to a regime with a nearly constant advancing and receding angles. In the latter regime, which we referred to as the macroscopic limit, the hysteresis amplitude is shown to be proportional to the defect force.

Finally, there are a number of interesting questions closely related to the analysis presented here. For example, extension of the static approach to investigate a microchannel configuration with nonidentical upper and lower walls. But also account for the influence of thermal noise, especially in the macroscopic limit, where the energy barriers which keep the system in metastable states are relatively low, something that is also revelant in the context of nanodefects [24,25]. Moreover, noise can induce dynamic/state transitions in rugged energy landscapes and further hysteresis effects (noise-induced hysteresis) [38,39]. Of particular interest will also be the corresponding dynamic study, addressing the question of how the hysteresis is amplified by the absolute velocity of the CL in each of the qualitatively differently different regimes of hysteresis. Extension of the present analysis to 3D configurations, though possible in principle, would require considering an infinite-dimensional generalization, which most likely will have to be treated numerically.

APPENDIX: OTHER CONFIGURATIONS

Here we briefly contrast the problem of a liquid-gas meniscus in a microchannel with that of a cylindrical droplet. Previous works on the statics of this configuration [7,20,40,41] have predicted hysteresis and stick-slip motion upon varying the volume of the droplet, similarly to the present work. Recently, this behavior has also been observed when the droplet is fed trough a pore [15].

In the cylindrical droplet configuration, the volume V of the droplet is, as for our microchannel, an explicit function of the contact line position x: $V = x^2 g(\theta)$, with $g(\theta)$ a geometric factor. A similar analysis as in Sec. III A would give as a criterion for a jump to occur the expression,

$$\frac{\partial \theta_i}{\partial x} = \hat{\theta}_{ic} = \frac{-2g(\theta_i)}{xg'(\theta_i)}, \tag{A1}$$

where $\frac{g(\theta_i)}{g'(\theta_i)}$ is positive for the physical range of θ_i. Thus, for this configuration $\hat{\theta}_{ic}$ is an explicit function of x, which was not the case for our microchannel prototype. Whether a defect is strong or weak will therefore depend on how far it is from the center of the droplet. Any defect which is far enough from the origin ($\hat{\theta}_{ic}$ close enough to zero) will induce hysteresis and therefore no threshold exists for sufficiently large droplets, just like in the macroscopic limit $\lambda \to 0$ for the microchannel.

Furthermore, Fig. 14 shows that, for a given periodic intrinsic contact angle distribution, upon increasing the volume of the droplet, the system passes through the same qualitatively different regimes of hysteresis (introduced in Sec. III B) as for the microchannel. We neglect any external noise, which would enable the system to cross energy barriers, and we assume that the droplet center does not shift during the process (see Ref. [15] for details). Upon increasing V (from left to right), the system goes from a subthreshold regime, through a regime with pronounced stick-slip, and finally to the macroscopic limit, for droplets much larger than the length scale of the heterogeneity. In both this configuration and that of the microchannel, the ratio of the gas-liquid interface length to the typical length scale of the heterogeneity seems to be an important physical parameter which determines the hysteresis behavior. In particular, a general conclusion seems to be that the
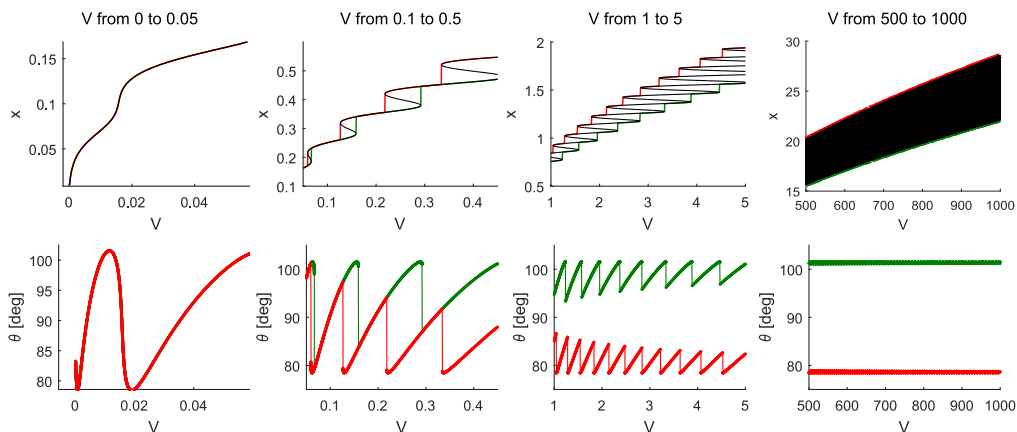
FIG. 14. Qualitatively different regimes of hysteresis for a droplet caused by a periodic heterogeneity described by Eq. (29) with $A_0 = 0.2$ and $\lambda = 0.1$ (assuming the system has no ability to overcome any energy barriers). The columns represent zooms on different ranges of V with qualitatively different behavior. The plotted quantities are the same as described in the caption of Fig. 9.

advancing and receding contact angles become independent of the particular liquid configuration (drop, meniscus, bubble,…) when this ratio becomes sufficiently large. In such macroscopic limit, the hysteresis range is fixed by the maximum and the minimum of the contact angle distribution, with the Cassie-Baxter angle falling in between, and stick-slip behavior is unobservable. This general conclusion supports the use of the common basic way of introducing CAH into static or time-dependent macroscopic models [3] by prescribing given constant values for the advancing and receding angles.

---

[1] P. G. de Gennes, Wetting: Statics and dynamics, Rev. Mod. Phys. **57**, 827 (1985).

[2] D. Bonn, J. Eggers, J. Indekeu, and J. Meunier, Wetting and spreading, Rev. Mod. Phys. **81**, 739 (2009).

[3] Y. Sui, H. Ding, and D.M. Spelt, Numerical simulations of flows with moving contact lines, Annu. Rev. Fluid Mech. **46**, 97 (2014).

[4] D. C. Pease, The significance of the contact angle in relation to the solid surface, J. Phys. Chem. **49**, 107 (1945).

[5] E. B. Dussan, On the spreading of liquids on solid surfaces: Static and dynamic contact lines, Annu. Rev. Fluid Mech. **11**, 371 (1979).

[6] J. F. Joanny and P. G. de Gennes, A model for contact angle hysteresis, J. Chem. Phys. **81**, 552 (1984).

[7] A. Marmur, Contact angle hysteresis on heterogeneous smooth surfaces, J. Colloid Interface Sci. **168**, 40 (1994).

[8] N. Savva and S. Kalliadasis, Two-dimensional droplet spreading over topographical substrates, Phys. Fluids **21**, 092102 (2009).

[9] N. Savva, S. Kalliadasis, and G. A. Pavliotis, Two-Dimensional Droplet Spreading Over Random Topographical Substrates, Phys. Rev. Lett. **104**, 084501 (2010).

[10] N. Savva, G. A. Pavliotis, and S. Kalliadasis, Contact lines over random topographical substrates. Part 2. Dynamics, J. Fluid Mech. **672**, 384 (2011).

[11] R. Vellingiri, N. Savva, and S. Kalliadasis, Droplet spreading on chemically heterogeneous substrates, Phys. Rev. E **84**, 036305 (2011).

[12] C. Wylock, M. Pradas, B. Haut, P. Colinet, and S. Kalliadasis, Disorder-induced hysteresis and nonlocality of contact line motion in chemically heterogeneous microchannels, Phys. Fluids **24**, 032108 (2012).

[13] N. Savva and S. Kalliadasis, Droplet motion on inclined heterogeneous substrates, J. Fluid Mech. **725**, 462 (2013).

[14] N. Savva and S. Kalliadasis, Low-frequency vibrations of two-dimensional droplets on heterogeneous substrates, J. Fluid Mech. **754**, 515 (2014).

[15] M. Pradas, N. Savva, J. B. Benziger, I. G. Kevrekidis, and S. Kalliadasis, Dynamics of Fattening and Thinning 2D Sessile Droplets, Langmuir **32**, 4736 (2016).

[16] H. B. Eral, D. J. C. M. 't Mannetje, and J. M. Oh, Contact angle hysteresis: A review of fundamentals and applications, Colloid Polym. Sci. **291**, 247 (2012).

[17] T. Cubaud and C. M. Ho, Transport of bubbles in square microchannels, Phys. Fluids **16**, 4575 (2004).

[18] R. E. Johnson and R. H. Dettre, Contact angle hysteresis. iii. Study of an idealized heterogeneous surface, J. Phys. Chem. **68**, 1744 (1964).

[19] E. Bittoun and A. Marmur, Chemical nano-heterogeneities detection by contact angle hysteresis: theoretical feasibility, Langmuir **26**, 15933 (2010).

[20] S. Brandon and A. Marmur, Simulation of contact angle hysteresis on chemically heterogeneous surfaces, J. Colloid Interface Sci. **183**, 351 (1996).

[21] X. Xu and X. Wang, Analysis of wetting and contact angle hysteresis on chemically patterned surfaces, SIAM J. Appl. Math. **71**, 1753 (2011).

[22] V. De Jonghe and D. Chatain, Experimental study of wetting hysteresis on surfaces with controlled geometrical and/or chemical defects, Acta Metall. Mater. **43** 1505 (1995).

[23] P. Collet, J. DeConinck, F. Dunlop, and A. Regnard, Dynamics of the Contact Line: Contact Angle Hysteresis, Phys. Rev. Lett. **79**, 3704 (1997).

[24] M. Delmas, M. Monthioux, and T. Ondarçuhu, Contact Angle Hysteresis at the Nanometer Scale, Phys. Rev. Lett. **106**, 136102 (2011).

[25] A. Giacomello, L. Schimmele, and S. Dietrich, Wetting hysteresis induced by nanodefects, Proc. Natl. Acad. Sci. USA **113**, E262 (2016).

[26] H. Perrin, R. Lhermerout, K. Davitt, E. Rolley, and B. Andreotti, Defects at the Nanoscale Impact Contact Line Motion at All Scales, Phys. Rev. Lett. **116**, 184502 (2016).

[27] P. G. de Gennes, F. Brochard-Wyart, and D. Quéré, *Capillarity and Wetting Phenomena: Drops, Bubbles, Pearls, Waves* (Springer, Berlin, 2004).

[28] J.-M. di Meglio and D. Quéré, Contact angle hysteresis: A first analysis of the noise of the creeping motion of the contact line, Europhys. Lett. **11**, 163 (1990).

[29] S. M. M. Ramos, E. Charlaix, A. Benyagoub, and M. Toulemonde, Wetting on nanorough surfaces, Phys. Rev. E **67**, 031604 (2003).

[30] J. Crassous and E. Charlaix, Contact angle hysteresis on a heterogeneous surface: Solution in the limit of a weakly distorted contact line, Europhys. Lett. **28**, 415 (1994).

[31] J.-M. di Meglio, Contact angle hysteresis and interacting surface defects, Europhys. Lett. **17**, 607 (1992).

[32] A. Marmur, Thermodynamic aspects of contact angle hysteresis, Adv. Colloid Interface Sci. **50**, 121 (1994).

[33] C. Priest, R. Sedev, and J. Ralston, A quantitative experimental study of wetting hysteresis on discrete and continuous chemical heterogeneities, Colloid Polym. Sci. **291**, 271 (2013).

[34] Y. J. Wang, S. Guo, H. Y. Chen, and P. Tong, Understanding contact angle hysteresis on an ambient solid surface, Phys. Rev. E **93**, 052802 (2016).

[35] S. Brandon, N. Haimovich, E. Yeger, and A. Marmur, Partial wetting of chemically patterned surfaces: The effect of drop size, J. Colloid Interface Sci. **263**, 237 (2003).

[36] A. Marmur and E. Bittoun, When Wenzel and Cassie are right: Reconciling local and global considerations, Langmuir **25** 1277 (2009).

[37] C. Priest, R. Sedev, and J. Ralston, Asymmetric Wetting Hysteresis on Chemical Defects, Phys. Rev. Lett. **99**, 026103 (2007).

[38] M. Pradas, D. Tseluiko, S. Kalliadasis, D. T. Papageorgiou, and G. A. Pavliotis, Noise Induced State Transitions, Intermittency, and Universality in the Noisy Kuramoto-Sivashinksy Equation, Phys. Rev. Lett. **106**, 060602 (2011).

[39] A. B. Duncan, S. Kalliadasis, G. A. Pavliotis, and M. Pradas, Noise-induced transitions in rugged energy landscapes, Phys. Rev. E **94**, 032107 (2016).

[40] M. Iwamatsu, Contact angle hysteresis of cylindrical drops on chemically heterogeneous striped surfaces, J. Colloid Interface Sci. **297**, 772 (2006).

[41] A. Marmur, Solid-surface characterization by wetting, Annu. Rev. Mater. Res. **39**, 473 (2009).